Journal of Industrial and Engineering Chemistry 114 (2022) 276–287

Contents lists available at ScienceDirect

Journal of Industrial and Engineering Chemistry

journal homepage: www.elsevier.com/locate/jiec

Camphene-derived hollow and porous nanofibers decorated with hollow NiO nanospheres and graphitic carbon as anodes for efficient lithium-ion storage

Jae Seob Lee [a], Rakesh Saroha [a], Jang Hyeok Oh [a], Chungyeon Cho [b], Bo Jin [c], Dong-Won Kang [d,*], Jung Sang Cho [a,*]

[a] Department of Engineering Chemistry, Chungbuk National University, Chungbuk 361-763, Republic of Korea
[b] Department of Carbon Convergence Engineering, College of Engineering, Wonkwang University, Iksan 54538, Korea
[c] Key Laboratory of Automobile Materials, Ministry of Education, and College of Materials Science and Engineering, Jilin University Changchun 130022, China
[d] School of Energy Systems Engineering, Chung-Ang University, Seoul 06974, Republic of Korea

ARTICLE INFO

Article history:
Received 7 April 2022
Revised 26 June 2022
Accepted 10 July 2022
Available online 16 July 2022

Keywords:
Electrospinning
Kirkendall diffusion
Camphene
Hollow nanostructure
Anodes

ABSTRACT

A synthesis strategy for hollow and porous nanofibers comprising hollow NiO (H-NiO) nanospheres formed via nanoscale Kirkendall diffusion and supported over a porous graphitic carbon matrix (H-NiO@HNFs) is reported herein to enable the fabrication of advanced anodes for stable lithium-ion batteries (LIBs). The H-NiO@HNFs comprising 1D longitudinal hollow channels ensured efficient diffusion of charged species via effective electrolyte percolation besides providing sufficient space to accommodate the large volume variations during repeated cycling. The hollow NiO nanospheres acted as chemical sites for lithiation and delithiation. Additionally, the H-NiO@HNFs exhibited improved lithium-ion storage properties, such as reasonable rate capability, stable prolonged cyclability at a high current density (1.0 A g^{-1}), and a high lithium-ion diffusion coefficient, primarily owing to their enhanced structural integrity compared to that of filled NiO nanofibers (F-NiO NFs). This facile synthesis approach could broaden the current understanding of 1D hollow nanostructures decorated with conventional hollow metal-oxide nanoparticles for various applications.

Introduction

Lithium-ion batteries (LIBs) remain the dominant power source for various portable electronics owing to their high available energy density, low cost, and environmental friendliness [1–3]. The increasing demand for long-life high-performance LIBs has intensified the development of novel electrode materials with controllable structures and morphologies. Transition metal oxides, such as oxides of cobalt, iron, nickel, and tin, have been explored as alternative LIB anode materials to the conventional graphite anode owing to their high theoretical capacities [4–16]. In particular, nickel oxide (NiO) has been extensively studied because of its high theoretical specific discharge capacity (718 mA h g^{-1}), environmental benignity, low cost, high chemical stability, and ease of synthesis [6,17–19]. However, the large volume variations during electrochemical processes result in pulverization of the electrode and, consequently, severe capacity fading [20]. Besides, the stoichiometric NiO is a wide-bandgap semiconductor (E_g = 3.6-eV) that results in low electrical conductivity (σ = 10^{-13} S cm^{-1}) [21,22].

The aforementioned issues, especially the severe volume variation, are being addressed by synthesizing hollow nanostructures with intrinsic morphologies, such as nanospheres [23], nanofibers [24], hollow-core–shell [25] and core–hollow-shell nanoparticles [26], thin shells [27], double-shell hollow microcubes [28], and multi-shell hollow microspheres [29]. In particular, the one-dimensional (1D) hollow nanostructure not only guarantees efficient electrolyte percolation via its longitudinal hollow channels, but also accommodates undesired volume changes, which alleviates the pulverization of electrodes and enables stable electrochemical performance [30–32]. Additionally, the 1D hollow channels decrease the effective diffusion length of the charged species, thus facilitating efficient charge transport through the

* Corresponding authors.
E-mail addresses: kangdwn@cau.ac.kr (D.-W. Kang), jscho@cbnu.ac.kr (J.S. Cho).

https://doi.org/10.1016/j.jiec.2022.07.017
1226-086X/

nanostructure. For example, Alcoutlabi et al. prepared multichannel hollow nanofibers (NFs) comprising TiO_2 and carbon by force-spinning an emulsion precursor solution [33]. As an LIB anode material, the resulting nanostructure exhibited a specific discharge capacity of 228.9 mA h g^{-1} after 100 cycles at a current density of 100 mA g^{-1}. Similarly, Ding et al. employed electrospinning to prepare $CoMn_2O_4$ hollow NFs through Ostwald ripening and the nanofibers showed a reversible capacity of 526 mA h g^{-1} after 50 cycles at a current density of 400 mA g^{-1} [32]. The low electrical conductivity of NiO has been addressed by employing it as a composite with a carbon framework [34–37]. However, a combined strategy of introducing hollow metal-oxide nanospheres and hollow NFs as a single entity has not been adopted, to the best of our knowledge.

Herein, we introduce an effective strategy to prepare 1D porous and hollow nanofibers with longitudinal hollow channels that were decorated with hollow NiO (H-NiO) nanospheres, which were surrounded by a graphitic carbon (GC) layer (H-NiO@HNFs). The hollow NFs were readily obtained through a one-pot conventional electrospinning technique using camphene that could sublime even at ambient temperature during spinning. The camphene molecules accumulated toward the center of the jet owing to the viscosity gradient between the outer and inner layers during surface solidification and subsequently sublimated, yielding a well-defined internal hollow nanostructure. The hollow NiO nanospheres that were well supported on the camphene-derived hollow NFs were similarly formed via nanoscale Kirkendall diffusion during heat treatment. Additionally, each hollow nanosphere was surrounded by a GC layer that facilitated rapid charge transfer during the charge/discharge process, leading to rapid reaction kinetics and a consequently improved electrochemical performance. Therefore, the nanostructure design approach presented herein is anticipated to enhance the current understanding of hollow nanostructures and enable realization of more sustainable and reliable electrodes for stable rechargeable-energy-storage systems.

Experimental section

Preparation of H-NiO@HNFs

The hollow NiO nanospheres supported on the camphene-derived hollow NFs with a GC matrix (H-NiO@HNFs) were readily prepared using a conventional electrospinning technique followed by a heat treatment, which enabled Kirkendall diffusion. Briefly, the spinning solution was prepared by sequentially dissolving camphene (7.0 g; Acros Organics, 75 %), $Ni(CH_3CO_2)_2{\cdot}4H_2O$ (5.0 g; Daejung, 97 %), and polyvinylpyrrolidone (3.0 g; PVP, Alfa Aesar; Mw: 1,300,000) in ethanol (50 mL; Duksan, 99.9 %) with continuous stirring overnight. The spinning solution was subsequently loaded into a plastic syringe pump (12 mL capacity) that was fitted with a 25-gauge stainless steel needle. The solution was fed through the needle at a flow rate of 1 mL h^{-1} onto a rotating drum (180 rpm) covered with aluminum foil as the collector. The applied voltage and the distance between the needle and collector were fixed at 20 kV and 20 cm, respectively. The as-spun Ni-salt/PVP/camphene nanofibers were stabilized at 150 °C for 24 h in a hot air oven and subsequently reduced at 400 °C for 3 h in a 5 % H_2 atmosphere. A final heat treatment was performed at 400 °C for 3 h in an air atmosphere to obtain hollow NiO nanospheres via Kirkendall diffusion, which were adequately supported over the hollow C nanofibers (H-NiO@HNFs). Moreover, a sample with filled NiO nanofibers (F-NiO NFs), that is, free from camphene and Kirkendall diffusion, was prepared for comparison using the aforementioned electrospinning technique and performing oxidation at 600 °C for 3 h.

Characterization

The morphologies of the as-prepared nanofibers were investigated by field-emission scanning electron microscopy (FE-SEM; Ultra Plus, ZEISS) and field-emission transmission electron microscopy (FE-TEM; JEOL, JEM-2100F, KBSI). The crystal structure and phase of the nanofibers were determined by X-ray diffraction (XRD; D8 Discover with GADDS, Bruker) using Cu Kα radiation (I = 1.5418 Å). The bonding and chemical environments of various elements in the nanofibers were determined by X-ray photoelectron spectroscopy (XPS; Thermo Scientific, K-Alpha) using monochromatic Al Kα radiation at 12 kV and 20 mA. Raman spectroscopy (Horiba Jobin-Yvon, HR800, LabRam) was employed to investigate the crystalline nature of the carbonaceous materials in the as-prepared nanofibers. The surface areas of the prepared nanofibers were estimated by N_2 adsorption–desorption isotherm analysis using the Brunauer–Emmett–Teller (BET) technique. Thermogravimetric analysis (TGA; Pyris 1, Perkin-Elmer) was performed to quantify the carbon content in the prepared nanofibers in an air atmosphere, unless otherwise mentioned, from room temperature to 600 °C at a step size of 10 °C min^{-1}.

Electrochemical measurements

CR2032-type coin cells were assembled to analyze the electrochemical performance of the prepared nanofibers. Working electrodes comprising the prepared nanofibers as the active material, Super-P as conductive carbon, and sodium carboxymethyl cellulose as a binder in a weight ratio of 7:2:1 were prepared using a slurry casting method on a copper foil and subsequently dried at 60 °C overnight in a hot air oven to remove the solvent. Metallic-Li and a microporous polypropylene film were used as the counter electrode and separator, respectively. $LiPF_6$ (1.0 M) in a blend of fluoroethylene carbonate and dimethyl carbonate (v/v = 1/1) was used as the electrolyte. The coin cells were assembled at room temperature in an Ar-filled glove box. The electrochemical performance of the prepared nanofibers was evaluated using cyclic voltammetry (CV) curves, charge–discharge profiles, and the Nyquist plots obtained via electrochemical impedance spectroscopy (EIS). The electrodes with mass loading ca. 1.0 mg cm^{-2} were used for these tests. The CV measurements were performed at a scan rate of 0.1 mV s^{-1}. The charge–discharge profiles of the nanofibers were obtained at various current densities (0.5–10.0 A g^{-1}), and the voltage window throughout the electrochemical tests was fixed at 0.001–3.0 V. The EIS data of the samples were collected in the frequency range of 100 kHz–0.01 Hz using a signal amplitude of 10 mV.

Results and discussion

A detailed schematic of the mechanisms involved in the H-NiO@HNFs synthesis is shown in Scheme 1. In particular, the difference in hydrophobicities of Ni salt, PVP, and camphene during electrospinning resulted in continuous (Ni-salt/PVP) and camphene-dispersed phases in ethanol (Scheme 1a-①). Additionally, the high vapor pressure of ethanol at ambient temperature led to rapid evaporation from the fiber surfaces, whereas the low vapor pressure of camphene molecules directed them toward the center of the jet stream [6]. This outward and inward diffusion of different molecules created a viscosity gradient at the outer and inner surfaces of the jet, which caused coagulation of the camphene molecules into an inner layer that sublimed at ambient temperature, thus forming a well-defined hollow interior space. Moreover, the strong coordination between the cyclic amide groups in PVP and the Ni^{2+} ions in the Ni salt led to the formation

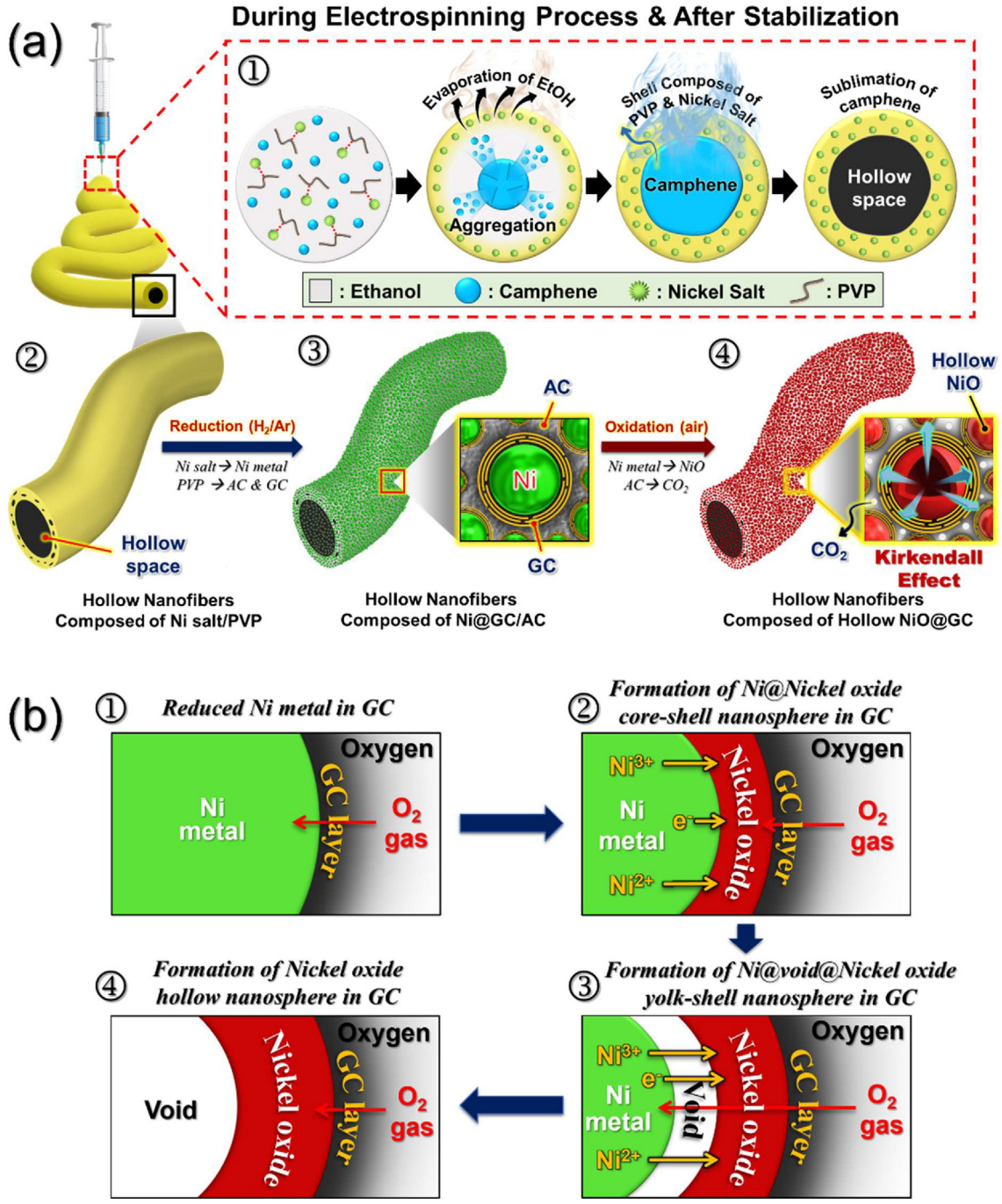

Scheme 1. (a) Detailed formation mechanism (①-④) of the camphene-derived 1D hollow GC nanofibers decorated with Kirkendall diffusion induced hollow-structured spherical NiO nanoparticles, and (b) formation mechanism of hollow nickel oxide nanospheres by Kirkendall diffusion effect in the surface region of a Ni nanosphere.

of a PVP/Ni-salt-rich shell surrounding the inner camphene layer, thus forming hollow NFs composed of Ni-salt/PVP after the electrospinning (Scheme 1a-②). During the heat treatment in a reductive atmosphere (5 % H_2/Ar) at 400 °C for 3 h, PVP was carbonized to amorphous carbon (AC), whereas the Ni salt was reduced to metallic Ni nanocrystals that were uniformly distributed throughout the AC matrix of the hollow NFs (Scheme 1a-③). Moreover, the AC present in the vicinity of the metallic Ni crystals transformed into GC owing to the catalytic nature of Ni. The selective conversion of AC to GC and the reduction led to the formation of Ni@GC/AC-composited hollow NFs (Scheme 1a-③), which were further oxidized at 400 °C for 3 h in an air atmosphere (Scheme 1a-④). The size of hollow metal-oxide nanoparticles is known to primarily depend on the size of the metallic nanocrystals, which in turn depends on the reduction and oxidation temperatures [38]. Moreover, a low treatment temperature guarantees the formation and homogeneous dispersion of non-agglomerated nanocrystals. Low-temperature oxidation led to the conversion of solid Ni nanocrystals into uniformly sized, evenly distributed hollow NiO nanospheres through a well-known nanoscale Kirkendall-diffusion-based mechanism (Scheme 1a-④). In particular, the oxidation of solid Ni nanocrystals yielded an intermediate Ni/NiO core–shell-type structure, which enhanced the outward diffusion of smaller Ni cations compared to the inward diffusion of O_2 gas molecules

upon further oxidation (Scheme 1b). This diffusion gradient led to the formation of Kirkendall voids, which produced hollow NiO nanospheres upon complete oxidation (Scheme 1a-④). Additionally, the AC in the composite hollow NFs was selectively decomposed into gaseous products that remained as GC only in the matrix. Overall, the hollow NiO nanospheres were successfully synthesized through Kirkendall diffusion and adequately supported in the camphene-derived hollow NFs with a porous GC matrix.

The morphological and phase-related changes of the prepared nanofibers after each synthesis step were analyzed to comprehensively elucidate the synthesis mechanism. The morphological, phase, and thermal stability characteristics of the as-spun hollow Ni-salt/PVP composite nanofibers, which were formed by sublimation of internal camphene and stabilized at 150 °C, are shown in Fig. 1. FE-SEM analysis (Fig. 1a) revealed a 1D fibrous morphology with an average diameter of ∼ 700 nm. Moreover, high-magnification cross-sectional image (Fig. 1b) clearly showed a well-defined hollow internal surface surrounded by an ∼ 150-nm-thick outer shell layer primarily consisting of PVP and Ni salt. The straightforward sublimation of camphene at ambient temperature (25–30 °C) during spinning facilitated the creation of a well-defined hollow internal structure of the fibers. XRD analysis (Fig. 1c) suggested that the amorphous-like phase primarily consisted of PVP and Ni-salt. The thermal stability of the stabilized nanofibers was investigated by TGA in an air atmosphere (Fig. 1d). The initial weight loss up to 100 °C is due to the removal of moisture or crystal water from the nanofibers. The second major weight loss (250–350 °C) is related to the decomposition of PVP into gaseous products via AC and that of Ni salt into nickel oxide nanoparticles. No appreciable change in weight was observed until 600 °C, suggesting complete formation of the pure NiO phase. Consequently, a temperature of 400 °C was selected for heat treatment to obtain phase-pure hollow NiO nanospheres that were supported on the camphene-derived hollow NFs.

A simple heat treatment of the stabilized nanofibers was performed at 400 °C in a slightly reductive (5 % H_2/Ar) atmosphere to obtain uniformly distributed metallic Ni nanocrystals decorated on the hollow NFs (Fig. 2). FE-SEM analysis (Fig. 2a) indicated that the fibrous morphology of the nanofibers (mean ø = ∼600 nm) remained intact even after the heat treatment. The decrease in nanofiber diameter was due to thermal contraction during heating. High-magnification FE-SEM analysis (Fig. 2b) further confirmed that the well-defined hollow NFs were decorated with evenly distributed metallic Ni nanocrystals throughout the fiber nanostructure. Additionally, a ∼ 100-nm-thick shell layer was observed. XRD analysis (Fig. 2c) yielded diffraction peaks corresponding to the metallic Ni crystal structure. Moreover, the average crystallite size of the metallic Ni nanocrystals was determined to be ∼ 7 nm using the Scherrer equation for the (111) diffraction peak. TEM analysis (Fig. 2d) corroborated these results based on the formation of well-defined hollow NFs (light grey region) comprising uniformly distributed and sparsely packed metallic Ni nanocrystals (black spots) with ∼ 100-nm-thick shells (dark region). The PVP in the composite nanofibers transformed into AC during the heat treatment, which restricted the growth of the metallic Ni nanograins surrounding them. Additionally, the nanofibers comprised mesopores between the Ni nanocrystals (Fig. 2e), which appeared upon the decomposition of PVP into AC. Moreover, the carbonaceous regions in the vicinity of the Ni nanocrystals were effectively converted into GC owing to the catalytic nature of Ni (Fig. 2f). This observation is consistent with the high-resolution TEM (HR-TEM)

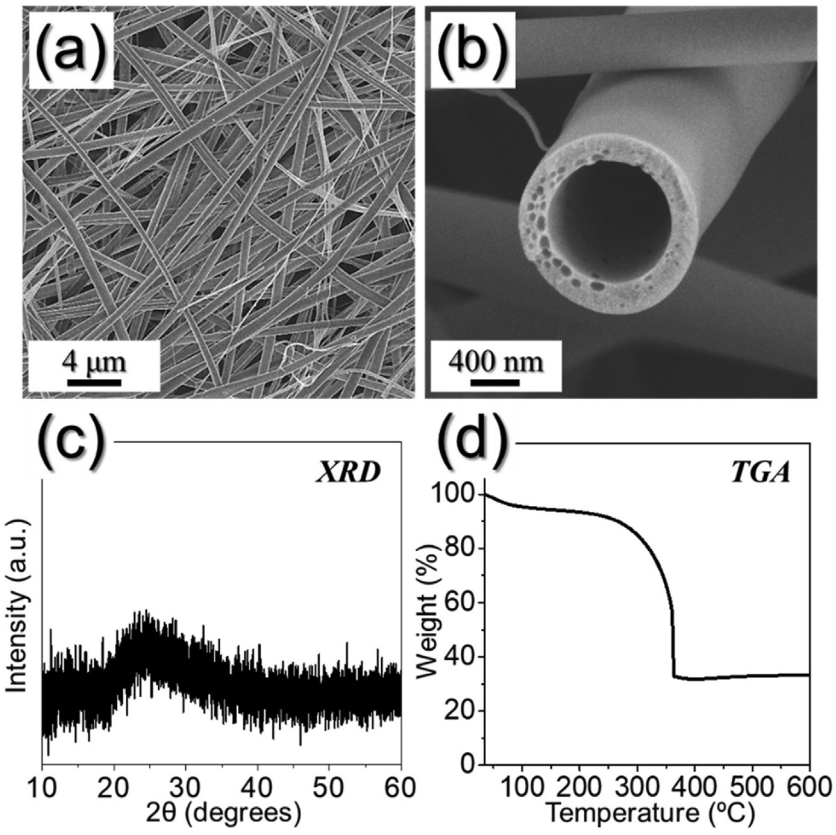

Fig. 1. Physical characterization of as-spun hollow nanofibers composed of Ni-salt/PVP formed by sublimation of internal camphene obtained after stabilization at 150 °C: (a) FE-SEM micrograph, (b) cross-sectional image, (c) XRD pattern, and (d) TG curve.

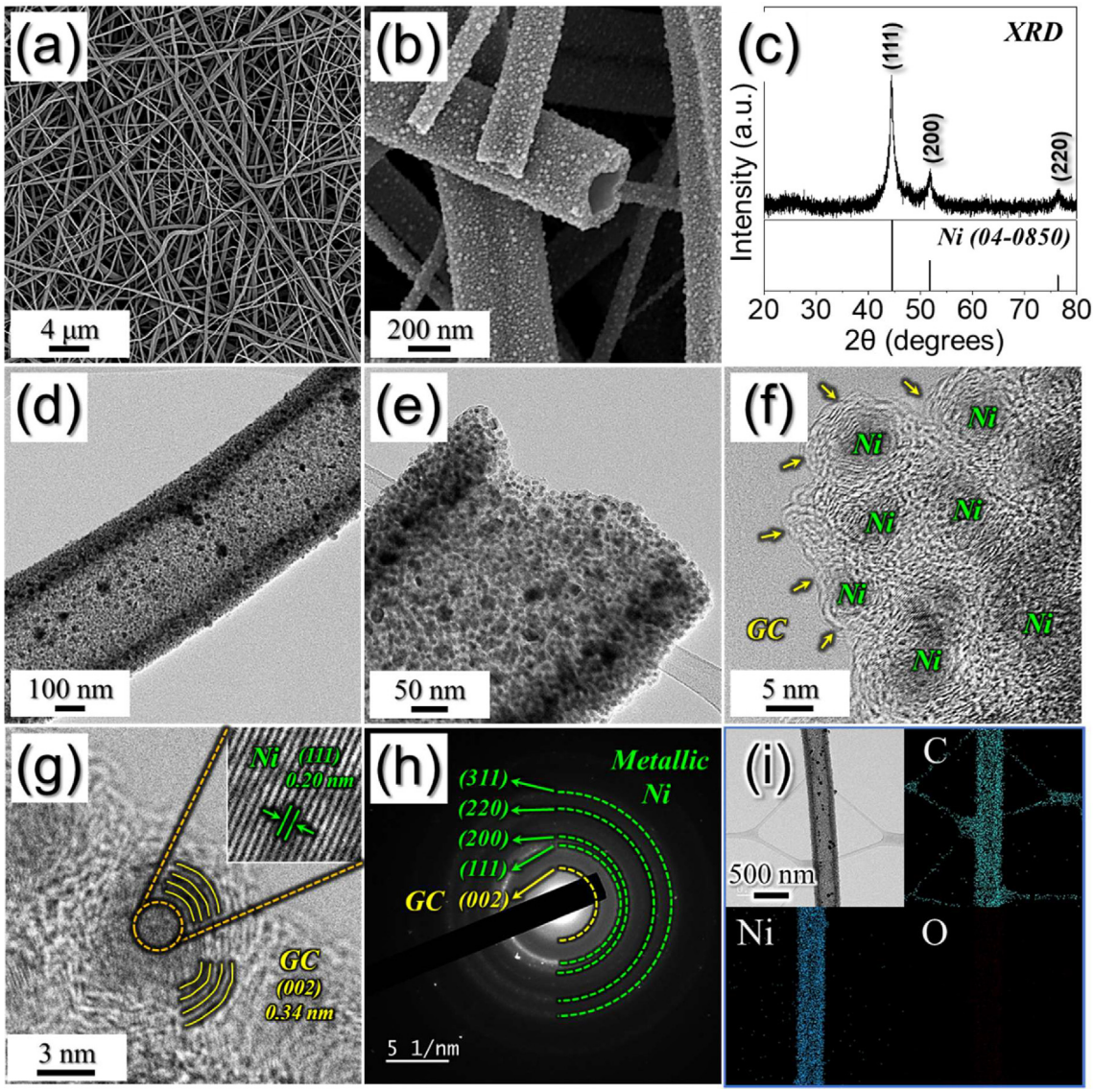

Fig. 2. Characterizations of hollow nanofibers composed of Ni@GC/AC obtained after the first heat-treatment of the as-stabilized nanofibers: (a,b) FE-SEM micrographs, (c) XRD pattern, (d-f) TEM images, (g) HR-TEM image, (h) SAED pattern, and (i) elemental dot mapping images.

image (Fig. 2g), which shows evenly distributed 7-nm-sized Ni nanocrystals uniformly surrounded by a GC layer. The clear lattice fringes with a separation of 0.20 and 0.34 nm (Fig. 2g) represented the (111) crystal plane of the metallic-Ni crystal structure and (002) plane of the GC, respectively. The selected area electron diffraction (SAED) pattern (Fig. 2h) reveals well-resolved diffraction rings corresponding to the crystal structure of metallic Ni and GC. Elemental mapping analysis (Fig. 2i) indicated uniform dispersion of C and Ni in the prepared nanofibers. Overall, the process of reduction yielded evenly distributed and nanosized metallic Ni nanocrystals that were uniformly surrounded by GC in the AC matrix of the camphene-derived hollow NF structure.

A second heat treatment was performed in an air atmosphere at 400 °C for 3 h to synthesize the hollow NiO nanoparticles that were supported by the GC-matrixed hollow NFs (Fig. 3). During oxidation, the metallic Ni nanocrystals transformed into the hollow NiO nanospheres via the nanoscale Kirkendall-diffusion-based mechanism described in Scheme 1a-④. In particular, the oxidation of solid Ni nanocrystals produced an intermediate Ni/NiO core–shell-type structure, which enhanced the outward diffusion of smaller Ni cations compared to the inward diffusion of O_2 gas molecules upon further oxidation [38]. This diffusion gradient created Kirkendall voids, which produced hollow NiO nanospheres upon complete oxidation. FE-SEM analysis (Fig. 3a and b) indicated that a 1D fibrous structure with a mean diameter of ~ 450 nm was retained, in addition to the well-defined hollow inner surface. Moreover, the shell layers with the uniformly sized NiO nanoparticles were clearly observed (Fig. 3b). The phase of the decorated nanoparticles was confirmed by XRD analysis (Fig. 3c), which showed well-resolved sharp peaks of the crystalline NiO phase only. Thus, the XRD results indicate complete phase conversion of metallic Ni into crystalline NiO. The average crystallite size of the NiO nanoparticles was calculated to be ~ 4 nm by applying the Scherrer equation to the (200) diffraction peak. TEM analysis (Fig. 3d) corroborated the presence of hollow NFs and the NiO nanoparticles that were evenly dispersed throughout the structure. High-magnification TEM analysis (Fig. 3e) confirmed the complete production of the hollow NiO nanospheres with well-developed Kirkendall voids. Additionally, pores were observed between the nanospheres because of the removal of AC to the gaseous products.

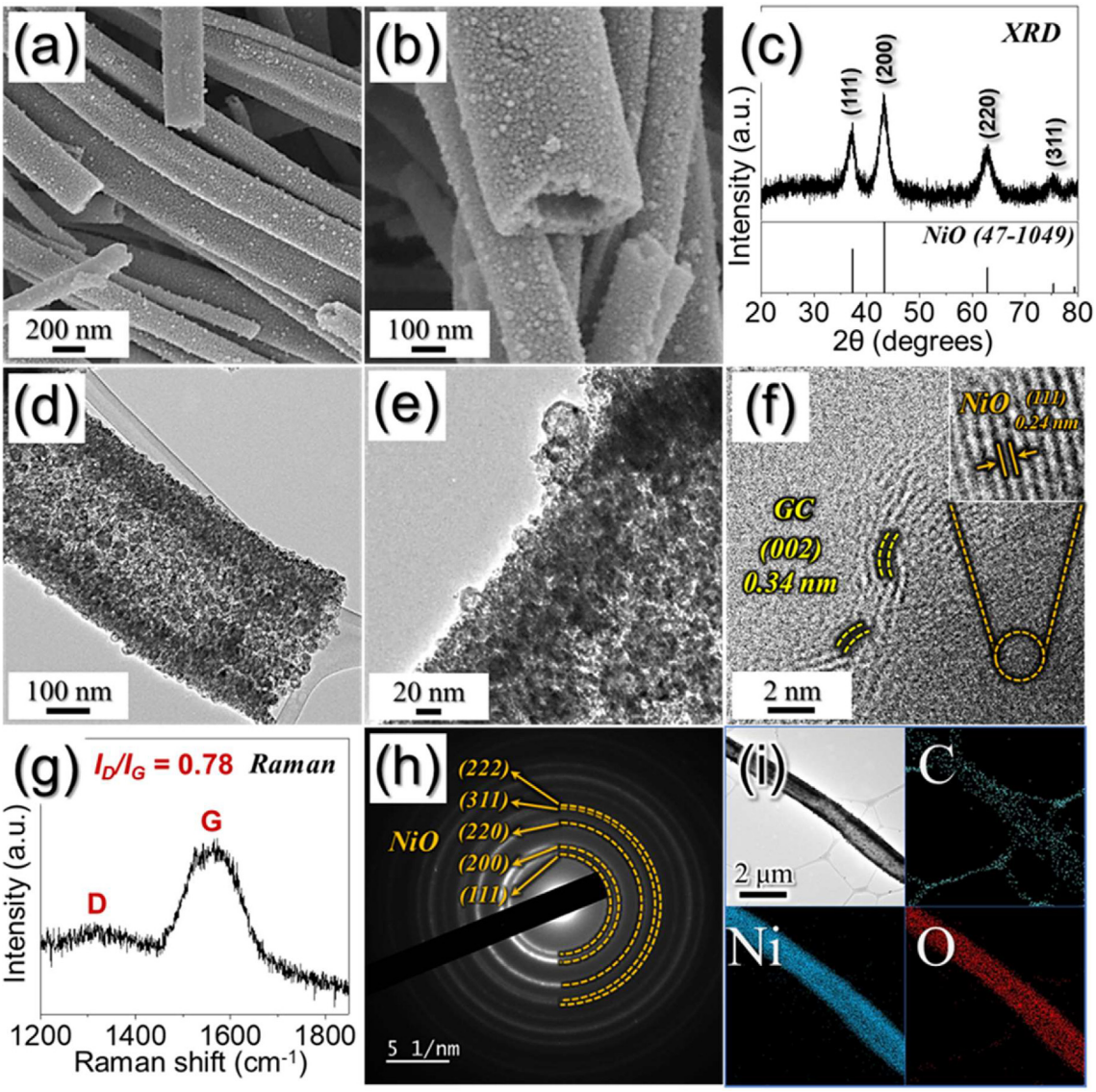

Fig. 3. Characterizations of H-NiO@HNFs obtained after the second heat-treatment at 400 °C for 3 h in air atmosphere: (a,b) FE-SEM micrographs, (c) XRD pattern, (d,e) TEM images, (f) HR-TEM image, (g) Raman spectrum, (h) SAED pattern, and (i) elemental dot mapping images.

The HR-TEM inset image in Fig. 3f shows lattice fringes separated by a distance of 0.24 nm, which correspond to the (111) crystal plane of the NiO phase; additionally, the lattice fringe of 0.34 nm appears corresponding to the (002) crystal plane of the GC, which surrounds the hollow NiO nanospheres. The crystallinity of the carbonaceous products in the prepared nanofibers was analyzed by Raman spectroscopy (Fig. 3g). The well-resolved low-intensity D and G bands located at 1323 and 1565 cm^{-1} with a relative intensity ratio (I_D/IG) of 0.78 validated the crystalline nature of the carbonaceous products, that is, GC in the prepared nanofibers [39]. The SAED pattern (Fig. 3h) showed diffraction rings corresponding to the nanocrystalline NiO crystal phase. Additionally, partial combustion of GC occurred during the oxidation heat treatment, so that a distinct ring pattern corresponding to GC was not observed. Elemental dot mapping analysis (Fig. 3i) indicated a uniform dispersion of Ni and O, suggesting the formation of NiO nanoparticles. Moreover, a sparse distribution of elemental C was observed, suggesting the presence of trace amounts of carbonaceous GC. Overall, oxidation enabled conversion of the solid metallic Ni nanocrystals into hollow NiO nanospheres via Kirkendall diffusion, which were uniformly wrapped by GC and decorated throughout the camphene-derived hollow NFs. Furthermore, an additional sample was synthesized using an identical electrospinning protocol to optimize the heat-treatment temperature for Kirkendall diffusion. The as-spun nanofibers obtained after stabilization were reduced at 400 °C and subsequently oxidized at a higher temperature (600 °C) for 3 h. The various characterization results of the resulting nanofibers, along with the relevant discussion, are provided in the Supplementary Material (Fig. S1).

The bonding states of various elements in the prepared H-NiO@HNFs were determined using XPS profiles (Fig. 4a), which showed photoelectron signals for the Ni 2p, C 1s, and O 1s s orbital states. The high-resolution Ni 2p XPS signal (Fig. 4b) showed two fitted peaks centered at 854.8 and 872.6 eV, corresponding to Ni $2p_{3/2}$ and Ni $2p_{1/2}$, respectively, in addition to three satellite peaks (denoted as "Sat.") at 861.2, 866.6, and 879.7 eV [40–42]. Furthermore, the deconvoluted Ni $2p_{3/2}$ and Ni $2p_{1/2}$ spectra showed further splitting, suggesting divalent (+2) and trivalent (+3) valence states for Ni, which is consistent with previously reported results [43–45]. Similarly, the C 1s XPS signal (Fig. 4c) was deconvoluted

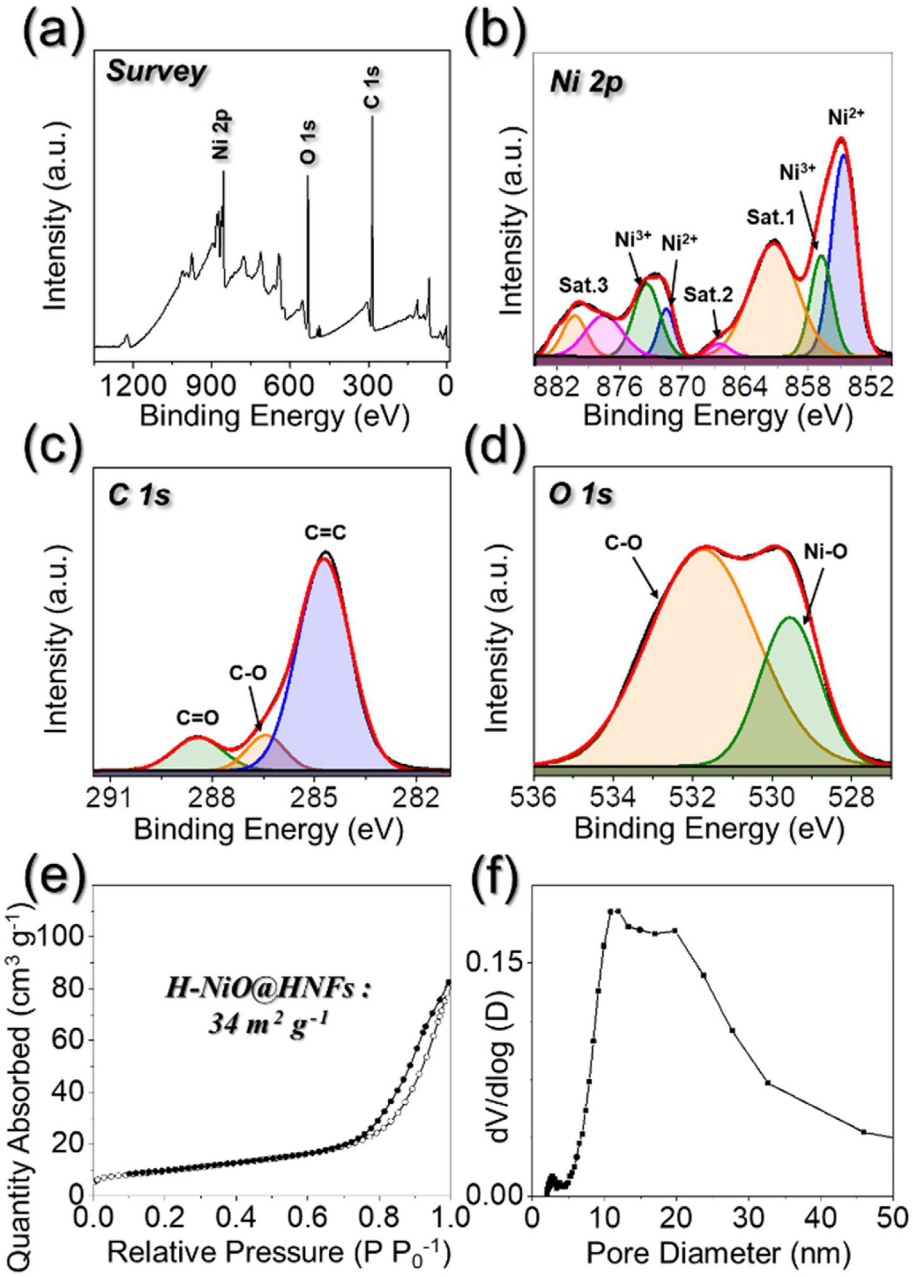

Fig. 4. (a) XPS survey spectrum, (b) Ni 2p XPS spectrum, (c) C 1 s XPS spectrum, (d) O 1 s XPS spectrum, (e) N_2 adsorption–desorption isotherms, and (f) BJH desorption pore size distribution curve.

into three well-fitted peaks at 284.7, 286.4, and 288.4 eV, corresponding to the C═C, C—O, and C═O bonds in the nanostructure, respectively [46–48]. The highly intense C═C peak suggested the presence of GC in the prepared nanofibers. A carbon content of ~ 3.0 wt%, primarily in the form of GC, was estimated by TGA (Fig. S2). The high-resolution O 1s XPS spectrum (Fig. 4d) showed two peaks corresponding to NiO and C—O bonds at 529.6 and 531.8 eV, respectively [49,50]. The BET surface area of the H-NiO@HNFs (Fig. 4e) was determined to be 34 m^2 g^{-1} and primarily attributed to the pores between the NiO nanoparticles that arose from the removal of AC and the hollow inner space of the nanofibers. This result is consistent with the pore size distribution curve (Fig. 4f), which showed two closely spaced peaks at 11 and 20 nm, mainly corresponding to the pores between the NiO nanoparticles.

The solid (or filled) NiO nanofibers (F-NiO NFs) were also prepared and analyzed in terms of their phases and morphological features for comparison (Figs. S3 and S4). A spinning solution comprising only Ni salt and PVP was electrospun, and the obtained nanofibers were stabilized at 150 °C and subsequently heat-treated in an air atmosphere at 600 °C for 3 h. FE-SEM analysis of the stabilized nanofibers (Figs. S3a and b) revealed a fibrous morphology (mean ø = 600 nm) with a smooth surface, indicating a well-composited Ni-salt/PVP matrix. The sample retained its fibrous morphology (Fig. S3c; average ø = 400 nm) upon oxidation at 600 °C. Additionally, the formation of densely packed, filled large grains of NiO was confirmed (Fig. S3d). The XRD pattern (Fig. S4a) displayed sharp and intense peaks that matched well with those of the NiO phase. Furthermore, the TGA curve

(Fig. S4b) indicated complete removal of carbonaceous products from the F-NiO NFs during oxidation. Additionally, the low BET surface area (1.6 m^2 g^{-1}; Fig. S4c), the near absence of pores, and the pore size distribution curve (Fig. S4d) indicated that the filled morphology led to porosity-free nanofibers.

The prepared H-NiO@HNFs were used as the working electrode in a CR2032-type coin cell and subjected to various electrochemical characterizations to validate their structural superiority (Fig. 5). The assembled cells were initially subjected to CV for five cycles in the voltage window of 0.001–3.0 V (vs Li^+/Li) at a voltage ramp rate of 0.1 mV s^{-1} (Fig. 5a). The small hump appearing in the first cathodic scan (0.83 V) corresponds to imperfections in the NiO nanograins due to the low-temperature heat treatment at 400 °C [9,38]. The subsequent strong peak at 0.43 V is due to the reduction of NiO to metallic Ni and the electrolyte decomposition that formed a solid electrolyte interphase (SEI) layer, in addition to the formation of amorphous Li_2O [38]. However, the cathodic peak at 0.43 V shifted to a higher potential of 1.03 V after the second cycle owing to the formation of ultrafine NiO nanocrystals during the redox process [38]. In contrast, the anodic scan showed two broad oxidation peaks at 1.46 and 2.26 V, which can be assigned to partial decomposition of the SEI layer and the subsequent oxidation of metallic Ni to NiO, in addition to the decomposition of Li_2O [9]. Furthermore, the overlapping CV profiles after the first cycle suggested the occurrence of highly reversible redox processes in the H-NiO@HNFs. The CV profiles of the F-NiO NFs (Fig. S5) showed similar redox characteristics. The CV profiles were further validated by conducting charge–discharge tests at a current density of 1.0 A g^{-1} (Fig. 5b). The H-NiO@HNFs displayed a discharge capacity of 1298 mA h g^{-1} and a Coulombic efficiency (CE) of 70.9 %. Additionally, the presence of well-distinguished charge–discharge plateaus is consistent with the CV results. In contrast, the F-NiO NFs exhibited a lower discharge capacity of 1115 mA h g^{-1} and a CE of 65.3 %. The trace amount of GC in the H-NiO@HNFs improved their electrical conductivity by functioning as an electron-transporting pathway, and the hollow NiO nanospheres enhanced the Li-ion-transport kinetics, which led to their higher CE [51]. The high discharge capacity of the H-NiO@HNFs was due to the presence of a hollow internal structure that not only provided short diffusion pathways for Li-ions, but also guaranteed more space to absorb the severe volume stress generated during the charge–discharge processes. Moreover, efficient electrolyte percolation enabled by the hollow longitudinal channels and numerous voids diminished the polarization effects. These results are consistent with the fact that the H-NiO@HNFs exhibited a lower polarization potential (ΔV = 1.54 V) than that of the F-NiO NFs (1.88 V). Therefore, the CV and initial charge–discharge results confirmed the enhanced electrochemical performance of the H-NiO@HNFs, which was primarily due to superior wetting of the electrodes and effective absorption of the severe volume stress generated during redox reactions.

The structural merits of the H-NiO@HNFs were further verified based on their cycling performance at 1.0 A g^{-1} (Fig. 5c). The H-NiO@HNFs displayed an initial discharge capacity of 1298 mA h g^{-1}, which stabilized at 861 mA h g^{-1} upon continuous cycling for 250 cycles. Additionally, the capacity increased up to approximately 110 cycles because of the kinetically activated electrolyte decomposition and the formation of a polymer-gel-like thin film owing

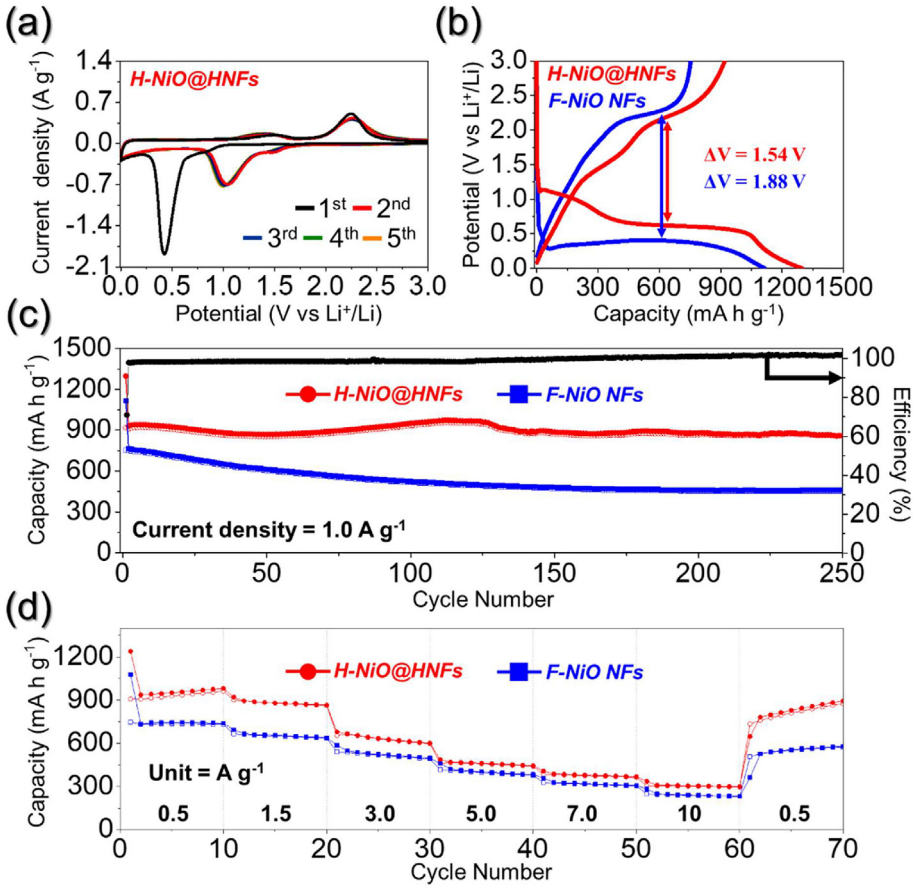

Fig. 5. Electrochemical properties of H-NiO@HNFs and F-NiO NFs: (a) CV curves of H-NiO@HNFs at 0.1 mV s^{-1} in the voltage window of 0.001–3.0 V, (b) initial discharge/charge curves at a constant current density of 1.0 A g^{-1}, (c) cycling performance at 1.0 A g^{-1}, and (d) rate capability test.

to the pseudocapacitive properties of NiO [52]. This phenomenon is frequently observed in conversion-reaction-based anode materials [53]. The cycling performance results indicate that the H-NiO@HNFs retained ~ 92 % of their capacity (measurements conducted after the 2nd cycle) with an average capacity decay rate of only 0.03 %. A high CE of 99.8 % indicated the occurrence of highly reversible electrochemical processes in the cell. In contrast, the F-NiO NFs displayed an initial discharge capacity of 1115 mA h g^{-1}, which monotonically decreased to 462 mA h g^{-1} up to the 250th cycle and subsequently plateaued, showing a capacity retention of ~ 60 % and an average capacity decay of 0.16 % per cycle. The high capacity retention and low capacity fading of the H-NiO@HNFs are primarily due to the effective accommodation of volume variation and the diminished polarization effects compared to those of the F-NiO NFs; this is because the filled architecture could not accommodate the volume variation and consequently enabled continuous capacity attenuation during the prolonged cycling.

Furthermore, rate capability tests were performed to authenticate the structural advantages of the H-NiO@HNFs at different current densities (0.5–10 A g^{-1}; Fig. 5d). The H-NiO@HNFs exhibited initial discharge capacities of 1239, 921, 679, 486, 408, and 336 mA h g^{-1} at current densities of 0.5, 1.5, 3.0, 5.0, 7.0, and 10.0 A g^{-1}, respectively. Additionally, the H-NiO@HNFs retained ~ 96 % of their capacity (i.e., 895 mA h g^{-1} from the 2nd cycle) at the aforementioned current densities when the current was reversed to 0.5 A g^{-1} In contrast, the F-NiO NFs exhibited lower initial discharge capacities of 1077, 694, 586, 458, 358, and 282 mA h g^{-1} at current densities of 0.5, 1.5, 3.0, 5.0, 7.0, and 10.0 A g^{-1}, respectively. Moreover, they retained only 78.6 % of their capacity (i.e., 735 mA h g^{-1}) when the current was reversed to 0.5 A g^{-1}. The improved rate capability of the H-NiO@HNFs is due to the presence of the hollow architecture, which acts as a 1D longitudinal channel for faster electron transport, and the interstitial nanovoids between the hollow NiO nanoparticles, which enable superior wetting of the electrode via efficient electrolyte percolation, thus guaranteeing rapid Li^+-ion diffusion processes. Similarly, the availability of sufficient space improves the volume expansion tolerance of the electrode, particularly at high rates and during prolonged cycling. In contrast, the dense nanostructure in the F-NiO NFs does not provide sufficient space to absorb the volume stress and consequently collapses (as discussed later), resulting in slow reaction kinetics. Moreover, the obtained electrochemical performance in the present work is comparable to the previous works, as presented in Table S1.

The electrochemical kinetics in the cells were further analyzed by acquiring CV profiles at different voltage scan rates (0.1–2.0 mV s^{-1}) in the voltage window of 0.001–3.0 V (Fig. 6a). The peak current (i) values during the reduction/oxidation processes were plotted against the respective scan rates (v) to differentiate between the surface- and diffusion-controlled reaction processes based on the following power-law relationship [5,48]:

$$i = a v^b \tag{1}$$

$$\log(i) = b \log(v) + \log(a) \tag{2}$$

where the variables a and b establish the surface- or diffusion-controlled nature of the process. The reaction process involved is capacitive or diffusion-controlled when b tends to 1.0 or 0.5, respectively [48]. The b values are generally determined using the slope of the log(i)–log(v) plots for different redox peaks in the CV curves. The b values corresponding to the different redox peaks of the H-NiO@HNFs and F-NiO NFs are shown in Fig. 6b and S6b, respectively. The b values for the three different redox

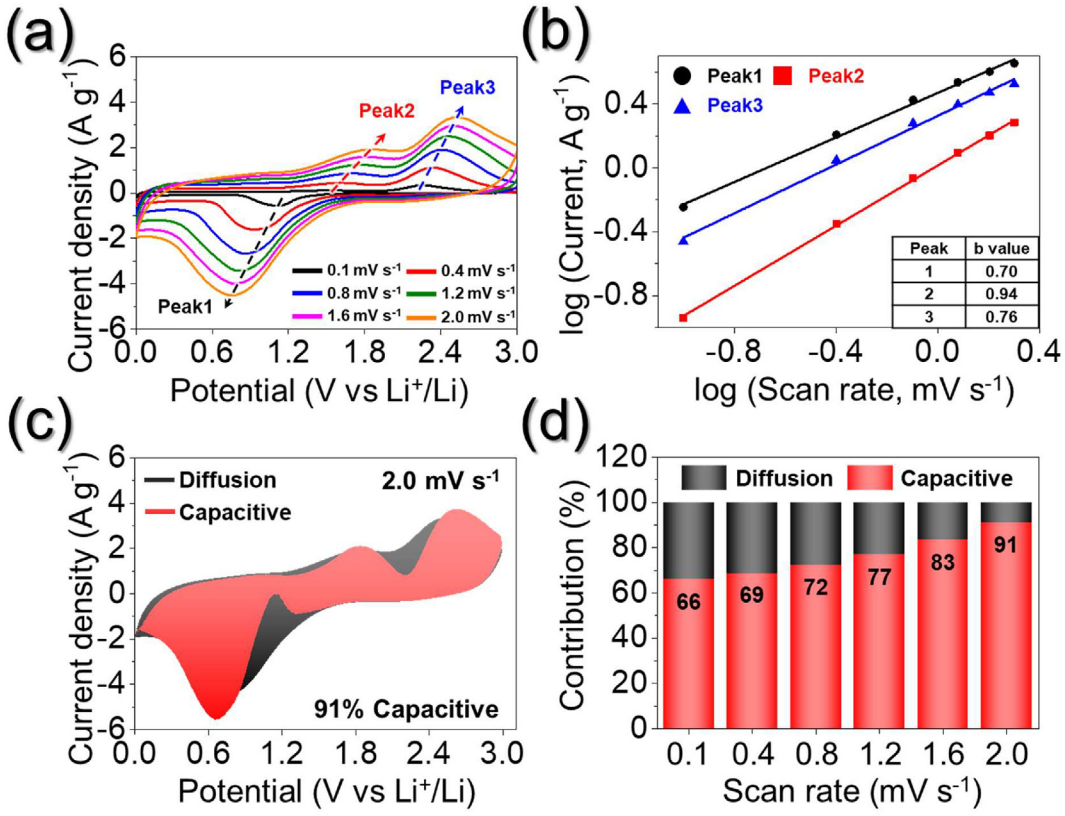

Fig. 6. Electrochemical reaction dynamics analysis of H-NiO@HNFs: (a) CV curves obtained at various scan rates, (b) current response (i) vs scan rate (n) at each redox peak, and (c) CV curves with the capacitive fraction shown by the red region at a scan rate of 2.0 mV s^{-1}, and (d) bar charts showing the percentage of the capacitive contribution at different scan rates.

peaks of the H-NiO@HNFs were 0.70, 0.94, and 0.76, implying a capacitive-controlled process. In contrast, the reaction dynamics of the F-NiO NFs (Figs. S6a and b) showed marginally lower *b* values, also indicating a capacitive-controlled redox process, but to a lesser extent. Typically, the reaction kinetics of an electrode material are closely related to the degree of the surface-controlled or capacitive effects, implying that a higher percentage of capacitive-controlled processes leads to enhanced transport kinetics. Therefore, the capacitive- and diffusion-controlled processes were separated from the total charge stored in the electrode material for quantitative analysis using the following equation [48]:

$$i = k_1 v + k_2 v^{1/2} \quad (3)$$

where k_1v and $k_2v^{1/2}$ represent the capacitive and diffusion contributions, respectively, and k_1 and k_2 are constants determined from the slope and intercept of the $i(V)/v^{1/2}$–$v^{1/2}$ curve, respectively [48]. The surface-controlled or capacitive contribution factor (i.e., k_1v) for the H-NiO@HNFs was ~ 91 % at a scan rate of 2.0 mV s^{-1} (Fig. 6c, red). Similarly, the hollow nanostructure showed relatively high proportions of the contribution from capacitive-controlled processes at all investigated voltage scan rates (Fig. 6d). In contrast, the F-NiO NFs exhibited a lower percentage of surface-controlled reaction contributions (Figs. S6c and d), even at a high scan rate of 2.0 mV s^{-1} (85 %). These results further confirmed the kinetically favored redox processes in the H-NiO@HNFs, which resulted in rapid Li-ion transport owing to the superior electrode wetting via the hollow structure and the efficient mitigation of volume variation during electrochemical processes.

The Nyquist plots of the assembled cells in a fully charged state were obtained using EIS measurements; the data were adequately fitted using a deconvoluted Randle-type equivalent-circuit model (Fig. S7) to elucidate the excellent Li-ion storage properties of the H-NiO@HNFs, as shown in Fig. 7. Furthermore, the measured resistance values of the two prepared structures were summarized in Table S2. The Nyquist plots for the fresh cells (Fig. 7a) showed analogous electrolyte resistance (R_e) values (19–26 Ω), indicating similar electrode–electrolyte interface reactions. However, the charge-transfer resistance (R_{ct}) values for the H-NiO@HNFs and F-NiO NFs were 173 and 317 Ω, respectively (Fig. 7a). The filled morphology of the F-NiO NFs led to poor electrolyte infiltration, which hindered charge transfer and led to a high R_{ct} value. Furthermore, a substantial decrease in R_{ct} for both samples was observed after the first

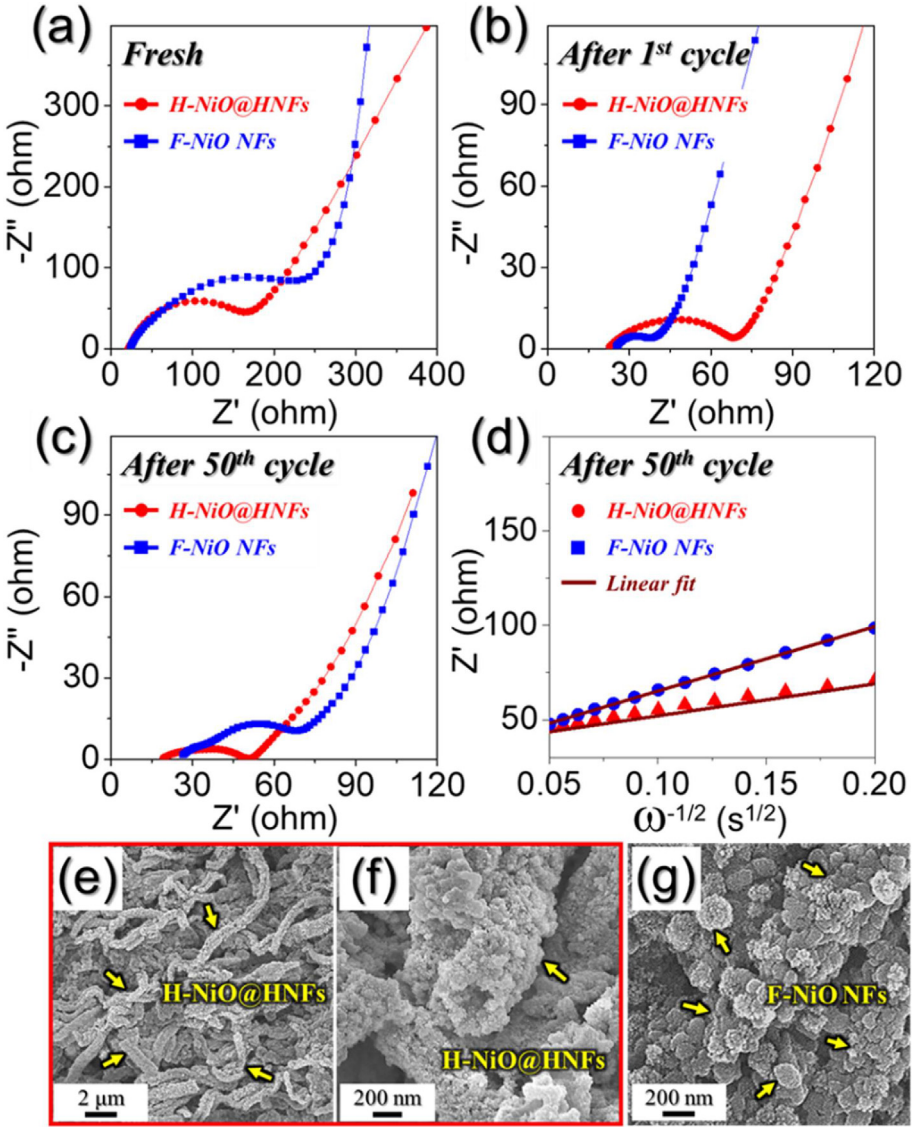

Fig. 7. (a-d) Nyquist impedance plots and (e-g) FE-SEM images of H-NiO@HNFs and F-NiO NFs obtained after 100th cycles at 1.0 A g^{-1}: (a) before cycling, (b) after 1st cycle, (c) after 50th cycle, (d) relationships between the real part of the impedance (Z_{re}) and $\omega^{-1/2}$ of the samples obtained after 50th cycles, (e, f) H-NiO@HNFs, and (g) F-NiO NFs.

cycle owing to the formation of ultrafine NiO nanocrystals in the structures [37,54]. The higher R_{ct} of the H-NiO@HNFs is attributed to its higher surface area than that of F-NiO NFs, which led to a slightly larger polarization [55,56]. The H-NiO@HNFs exhibited lower R_{ct} value (25 Ω) after the 50th cycle (Fig. 7c) compared to that of the F-NiO NFs (48 Ω), confirming the rapid redox kinetics and superior electrode integrity of the H-NiO@HNFs. To further validate the EIS results, the real part of the impedance (i.e., Z_{re}) was plotted as a function of $\omega^{-1/2}$ in the low-frequency region (Fig. 7d) and analyzed ($\omega = 2\pi f$; angular frequency). The H-NiO@HNFs showed a less steep slope at low frequencies, indicating higher Li-ion diffusivity in the hollow nanostructure than in the F-NiO NFs. These results confirmed the aforementioned electrochemical results. To verify the EIS results, Li-ion diffusion coefficients (D_{Li}^{+}) were calculated from Fig. 7d using the following equation [57]:

$$D_{Li^+} = \frac{0.5R^2T^2}{A^2F^4C^2\sigma_W^2} \quad (4)$$

where R is the gas constant, T is the temperature, A is the electrode area, C is the Li-ion concentration, F is the Faraday constant, and σ_W is the Warburg impedance factor. The D_{Li}^{+} value for the H-NiO@HNFs (4.61×10^{-14} cm^2 s^{-1}) was almost four times greater than that of the F-NiO NFs (1.20×10^{-14} cm^2 s^{-1}), indicating enhanced Li-ion diffusion and consequently improved redox reaction kinetics during the electrochemical processes. The higher diffusion coefficient for the H-NiO@HNFs further confirmed the structural robustness of the prepared hollow nanostructures, which enabled the high mechanical integrity of the electrode and guaranteed endurance to repeated cycling. The morphologies of all the electrodes that were cycled 100 times (1.0 A g^{-1}) were examined to confirm their structural robustness (Fig. 7e–g). FE-SEM analysis of the cycled H-NiO@HNFs (Fig. 7e and f) indicated that the nanostructures maintained their hollow morphology in addition to the continuous fibrous structure. High-magnification FE-SEM analysis (Fig. 7f) confirmed the high structural integrity of the prepared nanostructure. Furthermore, ex-situ XRD and XPS analysis were carried out for the cycled electrode (Fig. S8) to support the above results. The presence of pure NiO phase in the XRD pattern (Fig. S8a) even after prolonged cycling again suggests high structural integrity of the H-NiO@HNFs. Besides, high intensity peaks corresponding to the Cu current collector are also evitable. Furthermore, the XPS survey spectrum (Fig. S8b) of the cycled electrode display photoelectron signal corresponding to the F 1s and Li 1s at a binding energy of 685.1 and 55.8 eV, respectively, along with the Ni 2p, O 1s, and C 1s s signals [58–60]. The presence of Li 1s peak strongly indicates the existence of LiF/Li_2CO_3 (Fig. S8c) that formed due to electrolyte decomposition and subsequent formation of solid electrolyte interface, as reported previously [59–61]. Besides, the deconvoluted peak at 54.8 eV is attributed to the Li intercalation into the GC [62]. Likewise, the deconvoluted C 1s spectrum (Fig. S8d) also indicates the presence of various bonds that corresponds to different species usually present in SEI layer [59,61,63–65]. In contrast, the post-cycling morphology of the F-NiO NFs (Fig. 7g) suggested that the nanofibers could not withstand the severe volume variation during continuous cycling, which led to a complete collapse of the fibrous structure owing to its non-porous nature. These results validate the structural superiority of the H-NiO@HNFs, which not only provided 1D longitudinal hollow channels for the efficient diffusion of charged species, but also ensured effective electrolyte percolation. Moreover, the highly porous nanostructure comprising hollow NiO nanoparticles and hollow nanofibers provided sufficient space to accommodate the large volume variations during repeated cycling. Overall, the system containing hollow nanoparticles that were synthesized via a Kirkendall-diffusion-based mechanism and adequately supported on camphene-derived hollow NFs exhibited high structural integrity and superior electrochemical performance.

Conclusion

A novel synthesis strategy was designed to obtain porous nanostructures comprising hollow NiO nanospheres that were coated with GC via nanoscale Kirkendall diffusion and supported over camphene-derived hollow NFs; the nanostructures were applied as advanced anodes for stable LIBs. The hollow nanostructure guaranteed sufficient space to effectively accommodate the stress induced by severe volume variations, in addition to facilitating efficient wetting of the electrode through superior electrolyte percolation. The hollow NiO nanospheres acted as chemical sites for lithiation and delithiation. Enhancements in the overall electrochemical performance, such as reasonable rate performance and stable prolonged cycling, were achieved owing to the novel structural design. For instance, H-NiO@HNFs exhibited an initial discharge capacity of 1298 mA h g^{-1}, which stabilized at 861 mA h g^{-1} at the 250th cycle (~92 % of the capacity measured after the 2nd cycle), even at a high current density of 1.0 A g^{-1}; moreover, an average capacity decay rate of only 0.03 % and a high CE of 99.8 % were achieved. Therefore, the synthesis strategy reported herein is anticipated to provide substantial insight into the facile development of new hollow nanostructures for various energy-storage-related applications.

Declaration of Competing Interest

The authors declare that they have no known competing financial interests or personal relationships that could have appeared to influence the work reported in this paper.

Acknowledgements

This research was supported by Chungbuk National University Korea National University Development Project (2021)

Appendix A. Supplementary data

Supplementary data to this article can be found online at https://doi.org/10.1016/j.jiec.2022.07.017.

References

[1] R. Saroha, A.K. Panwar, Y. Sharma, P.K. Tyagi, S. Ghosh, Appl. Surf. Sci. 394 (2017) 25–36, https://doi.org/10.1016/j.apsusc.2016.09.105.
[2] R. Saroha, A. Gupta, A.K. Panwar, J. Alloys Compd. 696 (2017) 580–589, https://doi.org/10.1016/j.jallcom.2016.11.199.
[3] Y. Tan, Z. Jia, J. Sun, Y. Wang, Z. Cui, X. Guo, J. Mater. Chem. A 5 (2017) 24139–24144, https://doi.org/10.1039/C7TA08236C.
[4] S.H. Oh, S.M. Park, D.-W. Kang, Y.C. Kang, J.S. Cho, J. Ind. Eng. Chem. 83 (2020) 438–448, https://doi.org/10.1016/j.jiec.2019.12.017.
[5] J.S. Lee, M.S. Jo, R. Saroha, D.S. Jung, Y.H. Seon, J.S. Lee, et al., Small 16 (2020) 2002213, https://doi.org/10.1002/smll.202002213.
[6] J.H. Oh, M.S. Jo, S.M. Jeong, C. Cho, Y.C. Kang, J.S. Cho, J. Ind. Eng. Chem. 77 (2019) 76–82, https://doi.org/10.1016/j.jiec.2019.04.021.
[7] R. Saroha, A.K. Panwar, A.R. Farooq, L. Krishniya, P. Tyagi, Ionics 23 (2017) 2641–2650, https://doi.org/10.1007/s11581-017-2000-6.
[8] J.S. Cho, Y.J. Hong, Y.C. Kang, ACS Nano 9 (2015) 4026–4035, https://doi.org/10.1021/acsnano.5b00088.
[9] J.S. Cho, J.M. Won, J.-H. Lee, Y.C. Kang, Nanoscale 7 (2015) 19620–19626, https://doi.org/10.1039/C5NR05930E.
[10] J.S. Cho, Y.J. Hong, J.-H. Lee, Y.C. Kang, Nanoscale 7 (2015) 8361–8367, https://doi.org/10.1039/C5NR01391G.
[11] J.M. Won, J.H. Kim, Y.J. Choi, J.S. Cho, Y.C. Kang, J. Alloys Compd. 671 (2016) 74–83, https://doi.org/10.1016/j.jallcom.2016.01.252.
[12] R. Atchudan, B.G. Cha, N. Lone, J. Kim, J. Joo, Korean J. Chem. Eng. 36 (2019) 157–165, https://doi.org/10.1007/s11814-018-0200-z.

[13] L. Fan, P. Sun, L. Yang, Z. Xu, J. Han, Korean J. Chem. Eng. 37 (2020) 166–175, https://doi.org/10.1007/s11814-019-0414-8.
[14] E. Lim, J. Chun, C. Jo, J. Hwang, Korean J. Chem. Eng. (2021) 227–247, https://doi.org/10.1007/s11814-020-0693-0.
[15] R. Saroha, J.-H. Ahn, J.S. Cho, Korean J. Chem. Eng. (2021) 461–474, https://doi.org/10.1007/s11814-020-0729-5.
[16] Q.N. Tran, I.T. Kim, J. Hur, J.H. Kim, H.W. Choi, S.J. Park, Korean J. Chem. Eng. 37 (2020) 898–904, https://doi.org/10.1007/s11814-020-0506-5.
[17] H. Wu, M. Xu, H. Wu, J. Xu, Y. Wang, Z. Peng, et al., J. Mater. Chem. 22 (2012) 19821–19825, https://doi.org/10.1039/C2JM34496C.
[18] Y. Luo, M. Weng, J. Zheng, Q. Zhang, B. Xu, S. Song, et al., J. Alloys Compd. 750 (2018) 17–22, https://doi.org/10.1016/j.jallcom.2018.03.269.
[19] M.M. Rahman, S.-L. Chou, C. Zhong, J.-Z. Wang, D. Wexler, H.-K. Liu, Solid State Ionics 180 (2010) 1646–1651, https://doi.org/10.1016/j.ssi.2009.10.018.
[20] S.K. Meher, P. Justin, G. Ranga Rao, A.C.S. Appl, Mater. Interfaces 3 (2011) 2063–2073, https://doi.org/10.1021/am200294k.
[21] D. Adler, J. Feinleib, Phys. Rev. B 2 (1970) 3112, https://doi.org/10.1103/PhysRevB.2.3112.
[22] P. Lunkenheimer, A. Loidl, C. Ottermann, K. Bange, Phys. Rev. B 44 (1991) 5927, https://doi.org/10.1103/PhysRevB.44.5927.
[23] Z. Wang, L. Zhou, X.W. Lou, Adv. Mater. 24 (2012) 1903–1911, https://doi.org/10.1002/adma.201200469.
[24] D. Zhou, W.-L. Song, L.-Z. Fan, A.C.S. Appl, Mater. Interfaces 7 (2015) 21472–21478, https://doi.org/10.1021/acsami.5b06512.
[25] K. Zhao, M. Pharr, L. Hartle, J.J. Vlassak, Z. Suo, J. Power Sources 218 (2012) 6–14, https://doi.org/10.1016/j.jpowsour.2012.06.074.
[26] X. Li, L. Zhi, Nanoscale 5 (2013) 8864–8873, https://doi.org/10.1039/C3NR03197G.
[27] S. Xu, C.M. Hessel, H. Ren, R. Yu, Q. Jin, M. Yang, et al., Energy Environ. Sci. 7 (2014) 632–637, https://doi.org/10.1039/C3EE43319F.
[28] L. Zhou, D. Zhao, X.W. Lou, Adv. Mater. 24 (2012) 745–748, https://doi.org/10.1002/adma.201104407.
[29] X. Ma, Z. Wei, H. Han, X. Wang, K. Cui, L. Yang, Chem. Eng. J. 323 (2017) 252–259, https://doi.org/10.1016/j.cej.2017.04.108.
[30] Z. Han, B. Wang, X. Liu, G. Wang, H. Wang, J. Bai, J. Mater. Sci. 53 (2018) 8445–8459, https://doi.org/10.1007/s10853-018-2143-5.
[31] J. Xiang, X.-Y. Yu, U. Paik, J. Power Sources 329 (2016) 190–196, https://doi.org/10.1016/j.jpowsour.2016.08.079.
[32] G. Yang, X. Xu, W. Yan, H. Yang, S. Ding, Electrochim. Acta 137 (2014) 462–469, https://doi.org/10.1016/j.electacta.2014.05.167.
[33] L. Zuniga, V. Agubra, D. Flores, H. Campos, J. Villareal, M. Alcoutlabi, J. Alloys Compd. 686 (2016) 733–743, https://doi.org/10.1016/j.jallcom.2016.06.089.
[34] R.A. Susantyoko, X. Wang, Y. Fan, Q. Xiao, E. Fitzgerald, K.L. Pey, et al., Thin Solid Films 558 (2014) 356–364, https://doi.org/10.1016/j.tsf.2014.01.087.
[35] Y. Gong, M. Zhang, G. Cao, RSC Adv. 5 (2015) 26521–26529, https://doi.org/10.1039/C5RA01518A.
[36] E. Duraisamy, E. Sujithkrishnan, K. Kannadasan, P. Prabunathan, P. Elumalai, J. Electroanal. Chem. 887 (2021), https://doi.org/10.1016/j.jelechem.2021.115168 115168.
[37] M.S. Jo, S. Ghosh, S.M. Jeong, Y.C. Kang, J.S. Cho, Nano-Micro Lett. 11 (2019) 1–18, https://doi.org/10.1007/s40820-018-0234-0.
[38] J.S. Cho, S.Y. Lee, H.S. Ju, Y.C. Kang, A.C.S. Appl, Mater. Interfaces 7 (2015) 25641–25647, https://doi.org/10.1021/acsami.5b08793.
[39] R. Saroha, A.K. Panwar, J. Phys. D: Appl. Phys. 50 (2017), https://doi.org/10.1088/1361-6463/aa708c 255501.
[40] X. Hu, P. Li, X. Zhang, B. Yu, C. Lv, N. Zeng, et al., Nanomaterials 9 (2019) 1688, https://doi.org/10.3390/nano9121688.
[41] J.-W. Li, Q. Song, J.-B. Li, S.-C. Yang, Y.-S. Gao, Q. Wang, et al., Rare Met. 40 (2021) 1753–1761, https://doi.org/10.1007/s12598-020-01485-3.
[42] Á.A. Amaya, C.A. González, M.E. Niño-Gómez, F., Martínez, O,, J. Electron Spectrosc. Relat. Phenom. 233 (2019) 5–10, https://doi.org/10.1016/j.elspec.2019.03.007.
[43] J. Zhang, Q. Mei, Y. Ding, K. Guo, X. Yang, J. Zhao, et al., Mater. Interfaces 9 (2017) 29771–29781, https://doi.org/10.1021/acsami.7b08497.
[44] Y. Wang, L. Wang, B. Wei, Q. Miao, Y. Yuan, Z. Yang, et al., RSC Adv. 5 (2015) 100106–100113, https://doi.org/10.1039/C5RA20898J.
[45] A.A. Khaleed, A. Bello, J.K. Dangbegnon, M. Madito, O. Olaniyan, F. Barzegar, et al., J. Alloys Compd. 721 (2017) 80–91, https://doi.org/10.1016/j.jallcom.2017.05.310.
[46] R. Saroha, J.H. Oh, J.S. Lee, Y.C. Kang, S.M. Jeong, D.-W. Kang, et al., Chem. Eng. J. 426 (2021), https://doi.org/10.1016/j.cej.2021.130805 130805.
[47] R. Saroha, J.H. Oh, Y.H. Seon, Y.C. Kang, J.S. Lee, J.S. Cho, J. Mater. Chem. A 9 (2021) 11651–11664, https://doi.org/10.1039/D1TA01802G.
[48] J.S. Lee, R. Saroha, S.H. Oh, D.H. Shin, S.M. Jeong, J.K. Kim, et al., Small Methods 5 (2021) 2100195, https://doi.org/10.1002/smtd.202100195.
[49] A.N. Mansour, Surf. Sci. Spectra 3 (1994) 231–238, https://doi.org/10.1116/1.1247751.
[50] P. Yang, L. Li, S. Yu, H. Zheng, W. Peng, Appl. Surf. Sci. 493 (2019) 396–403, https://doi.org/10.1016/j.apsusc.2019.06.223.
[51] W. Yang, G. Cheng, C. Dong, Q. Bai, X. Chen, Z. Peng, et al., J. Mater. Chem. A 2 (2014) 20022–20029, https://doi.org/10.1039/C4TA04809A.
[52] F. Zhang, J. Yang, Emergent Mater. 3 (2020) 369–380, https://doi.org/10.1007/s42247-020-00080-7.
[53] Q. Li, G. Huang, D. Yin, Y. Wu, L. Wang, Part. Part. Syst. Charact. 33 (2016) 764–770, https://doi.org/10.1002/ppsc.201600084.
[54] J.H. Lee, S.H. Oh, S.Y. Jeong, Y.C. Kang, J.S. Cho, Nanoscale 10 (2018) 21483–21491, https://doi.org/10.1039/C8NR06075D.
[55] C. Wang, D. Wang, Q. Wang, H. Chen, J. Power Sources 195 (2010) 7432–7437, https://doi.org/10.1016/j.jpowsour.2010.04.090.
[56] J.S. Cho, J.-K. Lee, Y.C. Kang, Sci. Rep. 6 (2016) 1–13, https://doi.org/10.1038/srep23699.
[57] R. Saroha, A.K. Panwar, Y. Sharma, Ceram. Int. 43 (2017) 5734–5742, https://doi.org/10.1016/j.ceramint.2017.01.115.
[58] A.M. Andersson, D.P. Abraham, R. Haasch, S. Maclaken, J. Liu, K. Amine, J. Electrochem. Soc. 149 (2002) A1358–A1369, https://doi.org/10.1149/1.1505636.
[59] F. Jiang, L. Ma, J. Sun, L. Guo, Z. Peng, Z. Cui, et al., Mater. Interfaces 13 (2021) 14321–14326, https://doi.org/10.1021/acsami.1c01770.
[60] S. Leroy, H. Martinez, R. Dedryvère, D. Lemordant, D. Gonbeau, Appl. Surf. Sci. 253 (2007) 4895–4905, https://doi.org/10.1016/j.apsusc.2006.10.071.
[61] K.N. Wood, G. Teeter, A.C.S. Appl, Energy Mater. 1 (2018) 4493–4504, https://doi.org/10.1021/acsaem.8b00406.
[62] K.N. Wood, K.X. Steirer, S.E. Hafner, C. Ban, S. Santhanagopalan, S.-H. Lee, et al., Nat. Commun. 9 (2018) 2490, https://doi.org/10.1038/s41467-018-04762-z.
[63] J. Fondard, E. Irisarri, C. Courrèges, M.R. Palacin, A. Ponrouch, R. Dedryvère, J. Electrochem. Soc. 167 (2020), https://doi.org/10.1149/1945-7111/ab75fd 070526.
[64] A. Ponrouch, D. Monti, A. Boschin, B. Steen, P. Johansson, M.R. Palacín, J. Mater. Chem. A 3 (2015) 22–42, https://doi.org/10.1039/C4TA04428B.
[65] A. Darwiche, L. Bodenes, L. Madec, L. Monconduit, H. Martinez, Electrochim. Acta 207 (2016) 284–292, https://doi.org/10.1016/j.electacta.2016.03.089.